Spinodal decomposition and secondary phase formation in Fe-oversaturated GaN

G. Talut,* H. Reuther, J. Grenzer, A. Mücklich, A. Shalimov, and W. Skorupa
Institute of Ion Beam Physics and Materials Research, Forschungszentrum Dresden-Rossendorf e.V., P.O. Box 510119, 01314 Dresden, Germany

F. Stromberg
Fachbereich Physik, Universität Duisburg-Essen (Campus Duisburg), 47048 Duisburg, Germany
(Received 30 October 2009; revised manuscript received 1 February 2010; published 21 April 2010)

The flash-lamp annealing technique was applied to a GaN epilayer implanted with Fe in order to investigate the recovery of the crystal structure and the process of secondary phase formation. In the as-implanted state a spinodal decomposition occurs due to the oversaturation of Fe in GaN and a behavior similar to a spin glass is observed. Precipitation occurs even after annealing for the shortest annealing time of 3 ms. Iron nitrides as well as bcc-Fe are formed upon annealing for 20 ms and are responsible for the ferromagnetic response. No indication of the formation of a diluted magnetic semiconductor is observed. The correlation between the structure, magnetism and Fe-charge state was determined by x-ray diffraction, magnetometry and Mössbauer spectroscopy measurements.

DOI: 10.1103/PhysRevB.81.155212 PACS number(s): 75.50.Tt, 75.50.Lk, 75.50.Pp

I. INTRODUCTION

GaN is a wide band gap semiconductor that is attracting a lot of interest because of its potential field of applications like in optoelectronics, plasmonics, as well as for high power electronics. Doped with transition metals like Fe or Mn it also might become a diluted magnetic semiconductor (DMS) with a Curie temperature (T_c) above room temperature and be used for spintronics. Many experimental studies report about ferromagnetism at room temperature in Fe doped GaN. Generally, in a DMS, where magnetic atoms randomly substitute cation sites, ferromagnetism is supposed to be due to the indirect exchange coupling between magnetic impurities mediated by the holes.[1–4] Pacuski *et al.*[5] reported about the experimental observation of strong coupling effects in a diluted magnetic semiconductor $Ga_{1-x}Fe_xN$ with x less than 0.004. The authors expect robust ferromagnetism in the region of the insulator-to-metal transition for high hole densities. There are other possible sources of ferromagnetism like spinodal decomposition or ferromagnetic secondary phases. Bonanni *et al.*[6] prepared GaN:Fe layers by metalorganic chemical vapor deposition (MOCVD) and observed ferromagnetism which was partially attributed to the spinodal decomposition and nonuniform distribution of Fe-rich magnetic nanocrystals. Kuwabara *et al.*[7] reported formation of superparamagnetic nanoclusters in GaN:Fe epilayers prepared by RF-plasma-assisted molecular beam epitaxy. In case of ion implantation the reports from different groups are quite controversial. While Theodoropoulou *et al.*[8] and Shon *et al.*[9,10] reported ferromagnetism without observation of secondary phases we observed the formation of bcc-Fe nanoclusters after sample preparation at similar conditions. These clusters were the origin of ferromagnetic response.[11] Li *et al.* reported the coexistence of bcc-Fe and ε-Fe_3N in MOCVD prepared GaN:Fe films and pointed out the role of nitrogen pressure and structural disorder in the formation of Fe-rich phases during film growth.[12] Bonanni *et al.* had shown that the aggregation of magnetic ions in a semiconductor can be affected by the growth rate and doping with shallow impurities.[13] It is obvious that the engineering of certain material properties requires a thorough investigation and understanding of the impact of different preparation conditions on final results.

Using post implantation annealing techniques within seconds and minutes we observed the formation of mainly bcc-Fe clusters.[14] In this paper we investigate the whole process starting from the as-implanted state until the formation of crystalline clusters using even shorter annealing times.

II. EXPERIMENTAL

p-type (Mg) doped ($\sim 2\times10^{17}$ cm^{-3}) single crystalline wurtzite GaN(001) films of about 3 μm thickness epitaxially grown by metal organic vapor phase epitaxy (MOVPE) on sapphire (001) were used. The samples were tilted by 7° of normal relative to the ion beam to avoid channeling. They were implanted at room temperature with 195 keV Fe ions with a fluence $\Phi=8\times10^{16}$ cm^{-2} (sample 1) and $\Phi=16\times10^{16}$ cm^{-2} (sample 2) (both with $\Phi=6\times10^{16}$ cm^{-2} of ^{57}Fe, rest with ^{56}Fe), resulting in a maximum Fe concentration 9 and 18 at. % at the projected range $R_p=85$ nm, respectively, according to TRIM (Ref. 15). The high fluence was chosen in order to oversaturate the host material with magnetic impurities, since, based on the predictions made by Sato *et al.*,[16] the oversaturation might lead to higher T_c. In order to reduce implantation damage and phase separation the implanted samples were annealed in a flash-lamp annealing (FLA) chamber under constant Ar gas flow.[17] Annealing times in the ms range give the possibility to investigate the formation of metastable secondary phases due to rapid heating and cooling rates. Because of the lack of reference data for temperature measurement of the GaN surface during flash-lamp annealing, the known temperature on the Si surface was used as a reference, yielding about 1000 and 1200 °C for 3 and 20 ms annealing time, respectively (with about 70.9 and 232.3 J/cm^2, respectively). Due to some residual oxygen contamination an oxidation of samples was observed.

X-ray diffraction (XRD) measurements were performed at the Rossendorf beamline at the ESRF in Grenoble. ω-2θ scans were carried out using an x-ray energy of 10 keV. For the signal detection a scintillation counter was used. In order to increase the signal-to-background ratio to an acceptable level the acquisition time of the scintillation counter was set to 5 s per measurement point.

Selected samples were investigated by transmission electron microscopy (TEM). Rutherford backscattering spectrometry (RBS) in the channeling mode with 1.7 MeV He^+ was used to characterize the implantation region and the amount of damage caused by ion implantation and recovery after subsequent annealing. The concentration depth profiles of selected samples were recorded by Auger electron spectroscopy (AES). Conversion electron Mössbauer spectroscopy (CEMS) was applied to investigate the Fe lattice sites, electronic configuration and magnetism at room temperature. CEM spectra at RT were measured by placing the sample in a He-CH_4 gas flow proportional counter. CEM spectra at 4.2 K were taken by placing the sample in the inner evacuated tube of a liquid-helium bath cryostat and by using a channeltron detector. The spectra were evaluated with Lorentzian lines using the least-squares computer program NORMOS.[18] All isomer shifts are given with respect to bcc-Fe at RT. The investigations of the magnetic properties were performed with a Quantum Design MPMS superconducting quantum interference device (SQUID) magnetometer.

III. RESULTS AND DISCUSSION

FLA was applied with the intention to prevent or reduce the formation of secondary phases by deminishing the diffusion length. On the other hand the dopant activation as well as the solid phase epitaxial growth should occur. The diffusion length L of Fe in GaN can be estimated from the one dimensional solution of the second Fick's law by

$$L = 2\sqrt{D \cdot t} \tag{1}$$

with the diffusion coefficient D and time t. Azarov *et al.* calculated the bulk and near-surface diffusion coefficients for Fe in GaN with values of $D_{\text{bulk}} = 1 \times 10^{-15}$ cm^2 s^{-1} and $D_{\text{surface}} = 5 \times 10^{-15}$ cm^2 s^{-1}.[19] Bchetnia *et al.* determined the diffusion coefficient for V in GaN, which was comparable with the one from Fe and found the V diffusion activation energy E_A to be 2.9 ± 0.4 eV.[20] Using the Arrhenius equation

$$D = 1.5 \times 10^{-2} \text{ cm}^2 \text{ s}^{-1} \exp\left\{\frac{E_A}{k_B T}\right\} \tag{2}$$

given in Ref. 20, where k_B is the Boltzmann constant and T is the temperature, one can estimate the diffusion length for different temperatures and times during FLA. This yield $L_{1273\text{ K},3\text{ ms}} \approx 2.4 \times 10^{-10}$ m and $L_{1473\text{ K},20\text{ ms}} \approx 3.8 \times 10^{-9}$ m, going from atomic distances to sizes of small nanoclusters.

Figure 1 shows the ω-2θ XRD scans of GaN samples 1 and 2 after implantation and subsequent annealing for 3, 20, and 2×20 ms in Ar. No secondary phase formation was found in the pattern of as-implanted samples. The metastable ε-$Fe_{2.4}N$ was detected in the pattern of sample 1 after annealing for 3 ms. After 20 ms annealing a broad, but weak reflection appears at about 34.7° in the pattern of sample 1 and was identified as ε-$Fe_3N(111)$. This reflection is also present after 2×20 ms annealing. Another reflection appearing at about 33.9° cannot be assigned definitely and might be either ζ-$Fe_2N(102)$ or β-$Ga_2O_3(311)$. However, no other reflections were found to make the phase identification possible. In case of sample 2 [Fig. 1(b)] no reflections from secondary phases were found in the pattern after 3 ms annealing. Upon 20 ms annealing the formation of bcc-Fe is observed. However, after 2×20 ms annealing the reflection from bcc-Fe disappears, whereas a reflection at 34.7° appears, similar to the case of sample 1 after 20 ms annealing.

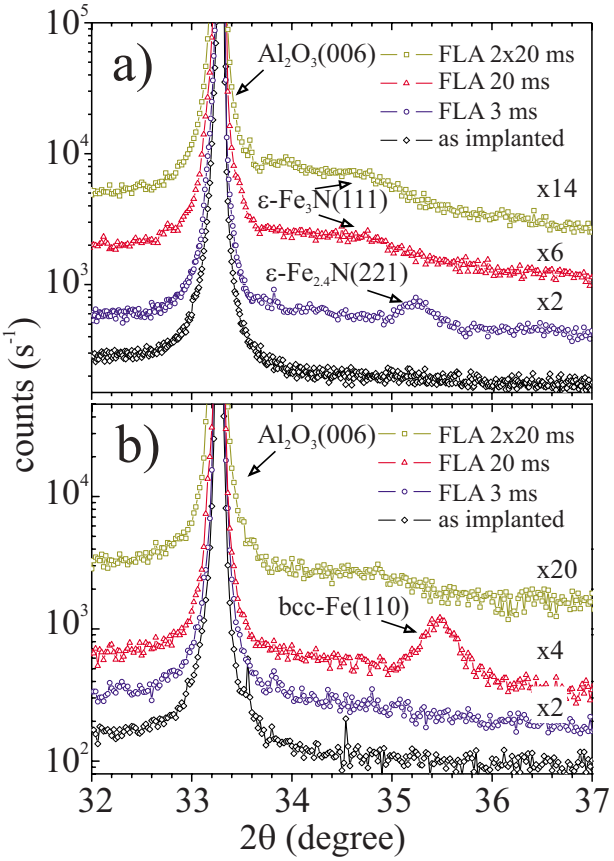

FIG. 1. (Color online) θ-2θ XRD scans of GaN samples implanted with (a) 8×10^{16} cm^{-2} and (b) 1.6×10^{17} cm^{-2} at RT, and subsequently annealed for 3 ms, 20 ms and 2×20 ms in Ar.

TEM investigations reveal an amorphization of samples within the first 60 nm starting from the surface. Still, some short range ordering of up to 1.5 nm in the as-implanted sample was still observable in TEM, which may serve as nucleation seeds for the (poly)-crystal growth during annealing [Fig. 2(a)]. In fact, TEM micrographs of selected samples after annealing show the presence of randomly oriented GaN crystallites of up to 15 nm [Fig. 2(b)] in size. In addition, up to 10 nm large bubbles were observed [Fig. 2(c)].

Figure 3 shows the AES concentration depth profiles of sample 2 after the implantation (a) and after subsequent annealing for (b) 3, (c) 2, and (d) 2×20 ms. In Fig. 3(a) sig-

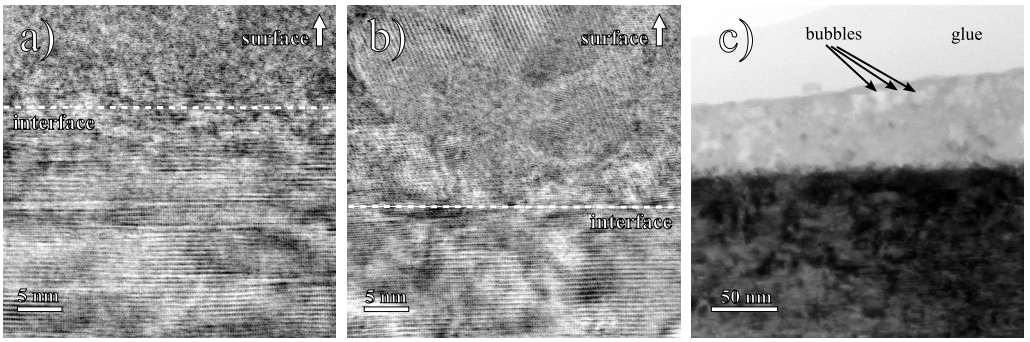

FIG. 2. TEM micrographs of sample 2 in as (a) implanted and (b) and (c) after 20 ms FLA.

nificant nitrogen loss is seen during the first 60 nm depth of GaN with a flat region between 15 and 45 nm. The loss of Ga and N can be explained by the dissolution of GaN upon ion radiation and evaporation. The range within the nitrogen loss occurs fits well with the amorphization range in GaN. The Ga-depth profile exhibits a minimum concentration at about 70 nm. In the crystalline bulk-GaN Ga is substituted by Fe and diffuses toward the surface during annealing. At the interface between the amorphous and crystalline region Ga starts to accumulate. Between 20 and 50 nm it also presents a flat concentration region. The Fe-implantation profile is controlled by sputtering, the integration yields about 6% Fe loss. A pronounced dip is clearly seen in Fe profile at about 60 nm, exactly at the amorphous/crystalline interface. Also in the Fe profile of sample 1 the minimum is located at 39 nm, again exactly at the amorphous to crystalline boundary (not shown). The minimum in Fe concentration has also been detected for Fe implantation at lower fluences, e.g., after the implantation with 3×10^{16} cm^{-2}. The dip is present at 16 nm depth. The presence of the minimum cannot be related to ballistic effects from ion implantation. There is no known measurement artifact explaining this behavior. Rather, the results suggest that the drop of Fe as well as of Ga concentrations at the interface depends on the density of the material. Implantation with high fluence is accompanied by the formation of defect clusters followed by N bubbles, resulting in high porosity and anomalous swelling of the implanted region.[21] Some recent studies report ion implantation induced disorder in GaN using Au or C (Refs. 22 and 23) ions. It is reasonable to assume that due to decomposition of GaN, the bubble formation starts to occur exactly at the interface between the crystalline and amorphous regions. This results in the formation of a low density layer. The layer structure can be divided into following regions starting from the surface: amorphous oxide layer, amorphous (Ga,Fe)N layer, low density amorphous (Ga,Fe)N layer, defective (Ga,Fe)N layer, and finally crystalline GaN. As a consequence, the position of the local minimum in the Fe concentration profile along with the starting decrease of N concentration can be used for the depth determination of the amorphous layer.

Upon annealing the concentration of Ga as well as of nitrogen decreases, accompanied by the simultaneous oxidation of Ga and Fe [see Figs. 3(b)–3(d)]. The oxidation rate of Ga is much higher than during annealing in pure O_2 reported by Lin *et al.*[24] However, Lin *et al.* used low-defective GaN wafers. Hence, our results can be explained by the reduced energy of decomposition of defective GaN and by the strong deficiency of nitrogen in the range of interest. N escapes upon annealing in N deficient atmosphere and is replaced by impurity oxygen. Due to oxygen contamination formation of β-Ga_2O_3 is expected for longer annealing times.[24]

Figure 4 shows the CEM spectra of sample 1 after implantation and subsequent annealing by FLA in Ar. The spectrum of the as-implanted sample [Fig. 4(a)] was fitted by using a singlet S for metallic Fe^0 with isomer shift $\delta = -0.10$ mm s^{-1}, a value similar to fcc-Fe and two quadrupole doublets D_{III} and D_{IV} for ionic Fe^{3+} with three and four nearest N neighbors, respectively.[25] The hyperfine parameters are summarized in Table I. For RT spectra of the annealed samples a similar fitting model was used. However, a significant change is observed in the spectrum after the 3 ms annealing [Fig. 4(b)]. The relative area of the doublet D_{III}

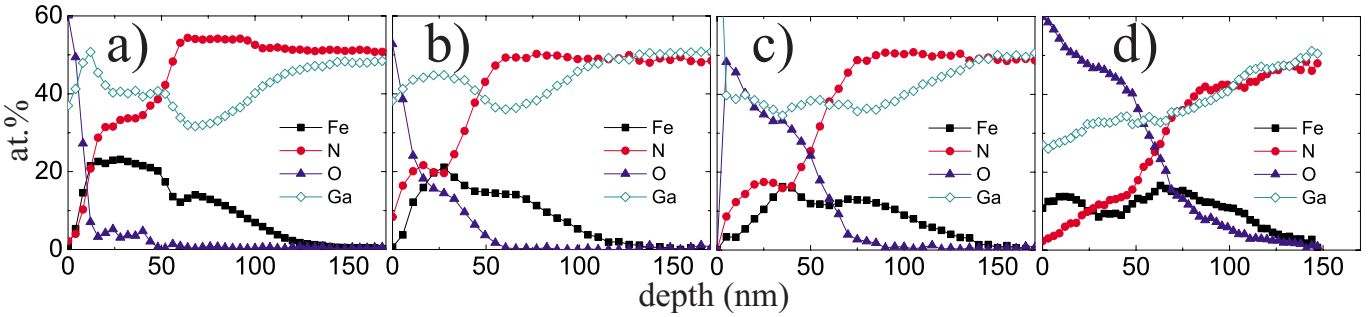

FIG. 3. (Color online) AES depth profiles of GaN sample series 2 (1.6×10^{17} cm^{-2}) implanted at RT (a) and subsequently annealed for (b) 3 ms, (c) 20 ms, and (d) 2×20 ms in Ar.

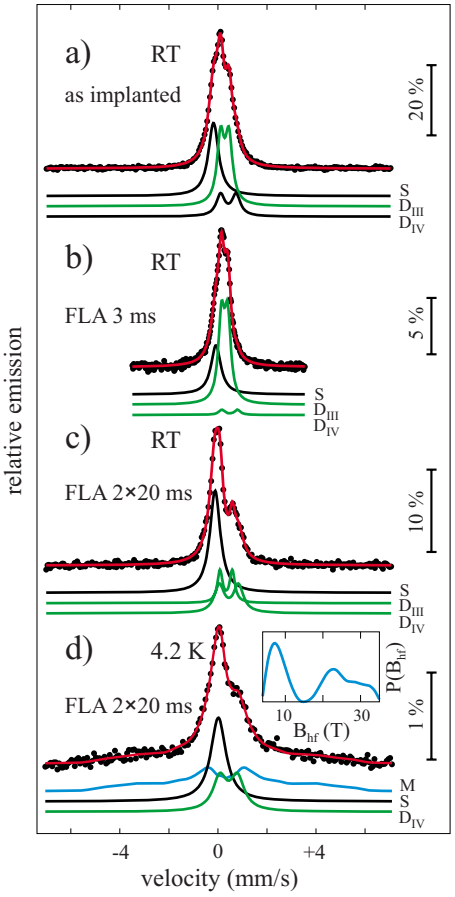

FIG. 4. (Color online) CEM spectra of the GaN sample series 1 (8×10^{16} cm^{-2}) implanted at RT (a) and subsequently annealed by FLA in Ar for (b) 3 ms, (c) and (d) 2×20 ms. (a)–(c) are recorded at RT and (d) at 4.2 K. The inset represents the probability distribution P(B_{hf}) for the magnetic hyperfine fields.

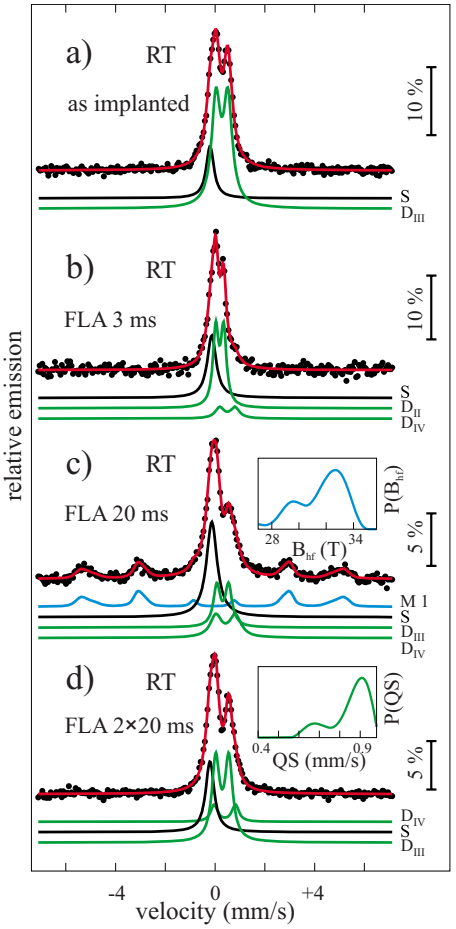

FIG. 5. (Color online) Room temperature CEM spectra of the GaN sample series 2 (1.6×10^{17} cm^{-2}) implanted at RT (a) and subsequently annealed by FLA in Ar for (b) 3, (c) 20, and (d) 2×20 ms. The insets represents the probability distributions P(B_{hf}) for the magnetic hyperfine fields and P(QS) for the quadrupole splittings.

increased strongly, accompanied by a lowering of the respective quadrupole splitting. This is related to the formation of paramagnetic ε-$Fe_{2.4}N$. After 20 ms annealing the quadrupole splitting of this doublet increases, accompanied by a reduction of the relative area. At the same time the relative areas of the other components increase. The spectrum does not change appreciable after 2×20 ms annealing [Fig. 4(c)]. This result agrees well with the XRD findings. The spectrum of the same sample, recorded at 4.2 K, revealed the presence of a subspectrum with magnetic hyperfine field distribution. The maxima of the distribution [inset in Fig. 4(d)] are well matched to the values characteristic of ε-$Fe_{3-x}N$.[26] The isomer shifts of all components are moved to positive values due to the second order doppler shift at 4.2 K. The broad linewidths of some spectral components can be explained by size or relaxation effects.

The as-implanted sample 2 exhibits a spectrum different from that of sample 1 [Fig. 5(a)]. Therefore it was fitted by a singlet S and a doublet D_{III}. The difference can be explained by the higher (structural) disorder caused by the higher fluence. This sample was also studied at 4.2 K (not shown). Besides of the change in isomer shift, related to the second order Doppler shift, no other changes in the spectrum were observed, in particular no appearance of magnetic hyperfine fields. The spectrum of the 3 ms annealed sample was again fitted by two doublets [Fig. 5(b)]. However, this time, a doublet D_{II} was used instead of D_{III}. This change in electronic configuration is an indication of phase separation or change. After the 20 ms annealing a magnetic hyperfine-split pattern is present in the spectrum [Fig. 5(c)]. According to the findings from XRD, the fit was modified by a hyperfine field distribution representing a bcc-Fe-like coordination. The relative spectral area of the distribution amounts to about 23.7%. This means, together with the relative area of the singlet of 37.6%, that 61.3% of Fe are in metallic state. However, the component related to the singlet is not ferromagnetic but paramagnetic. After 2×20 ms annealing the shape of the CEM spectrum changes due to the oxygen contamination and the fit has to be modified [Fig. 5(d)]. Since no ferromagnetic sextets at RT were detectable, the spectrum was fitted by paramagnetic doublets. It is supposed that the size of the bcc-Fe nanoclusters is reduced due to the oxidation and formation of an oxide shell. Therefore the magnetic behavior should be dominated by the rapid spin relaxation. In this case no magnetic hyperfine splitting is expected. Instead, depending on the crystalline symmetry, either a singlet for

TABLE I. Hyperfine parameters obtained from the evaluation of the Mössbauer spectra. Φ: fluence [$\times 10^{16}$ cm^{-2}], δ: isomer shift, Δ: quadrupole splitting, Γ: line width, A: relative area of each component with the statistical error of last digit given in parentheses, S: singlet, D: doublet or doublet distribution (dist.), M: magnetic hyperfine field distribution.

Φ	Annealing	Component	δ (mm/s)	Δ (mm/s)	Γ (mm/s)	A (%)
8	As-impl.	S (Fe^0)	−0.10		0.51	36.7(1)
		D_{III} (Fe^{3+})	0.36	0.34	0.35	45.6(2)
		D_{IV} (Fe^{3+})	0.51	0.64	0.42	17.7(2)
8	3 ms	S (Fe^0)	0.0		0.49	31.3(2)
		D_{III} (Fe^{3+})	0.35	0.26	0.31	64.9(2)
		D_{IV} (Fe^{3+})	0.56	0.65	0.29	3.8(2)
8	20 ms	S (Fe^0)	−0.04		0.55	56.0(1)
		D_{III} (Fe^{3+})	0.38	0.49	0.26	13.0(2)
		D_{IV} (Fe^{3+})	0.50	0.76	0.44	31.0(2)
8	2×20 ms	S (Fe^0)	−0.04		0.52	55.3(2)
		D_{III} (Fe^{3+})	0.41	0.51	0.26	16.7(4)
		D_{IV} (Fe^{3+})	0.53	0.79	0.49	28.0(4)
8[a]	2×20 ms	S (Fe^0)	0.10		0.75	34.3(2)
		D_{IV} (Fe^{3+})	0.52	0.72	0.68	24.5(2)
		M (Fe^{3+})	0.41	0.00	0.49	41.2(2)
16	As-impl.	S (Fe^0)	−0.10		0.38	18.1(2)
		D_{III} (Fe^{3+})	0.37	0.48	0.42	81.9(2)
16	3 ms	S (Fe^0)	−0.05		0.42	32.9(4)
		D_{II} (Fe^{3+})	0.29	0.28	0.26	53.7(4)
		D_{IV} (Fe^{3+})	0.46	0.81	0.44	13.4(4)
16	20 ms	S (Fe^0)	−0.03		0.52	37.6(2)
		D_{III} (Fe^{3+})	0.40	0.47	0.33	20.4(2)
		D_{IV} (Fe^{3+})	0.52	0.78	0.55	18.3(2)
		M1 (Fe^0)	0.02	−0.05	0.30	23.7(2)
16	2×20 ms	S (Fe^0)	−0.10		0.41	29.2(2)
		D_{III} (Fe^{3+})	0.40	0.52	0.37	59.8(2)
		D_{IV} (Fe^{3+})	0.49	Dist.	0.30	11.0(2)

[a]recorded at 4.2 K.

cubic symmetry (bcc-Fe) or a quadrupole doublet for hexagonal coordination (ε-$Fe_{3-x}N$) are expected. Hence, ε-$Fe_{3-x}N$ is represented by the quadrupole doublet D_{III} and has the largest contribution to the spectrum. The doublet D_{IV} is related to iron oxides. Surprisingly, the negative isomer shift of the singlet δ=−0.10 mm/s hints at the fcc-Fe-like site location, instead of the bcc-like. It can be assumed that the reduced volume of iron and lattice stress play a dominant role in the fcc-Fe phase synthesis.[27] Field-cooled/zero-field-cooled (FC/ZFC) SQUID measurements were performed in a 50 Oe field. Figure 6(a) shows the respective scans from sample 1 before and after subsequent annealing. The separation between the FC and ZFC curves is present in every scan. For the as-implanted sample the curves approach at about 8 K, but for the samples annealed for ≥20 ms the separation reaches RT. In general, the local maximum in the ZFC curve is a certain proof for clusterlike behavior, and represents the superparamagnetic blocking temperature. In some scans (e.g., after 3 ms annealing [Fig. 6(a)]), however, the local maxima in the ZFC curves were not observed. The absence of maxima might mislead the interpretation of the results. In fact, in the literature the absence is often regarded as a feature of diluted magnetic semiconductor. However, the missing maxima can also be explained as follows. The postimplantation annealing usually leads to clusters with a certain size distribution, with the consequence of a distribution of the blocking temperature. For the size distribution starting from the spinodal decomposition the maximum in the blocking temperature can be just at about some K. The results presented here seem to prove this suggestion. With longer annealing times the maximum in the ZFC curve moves toward higher temperature values—the clusters grow. The field dependent magnetization measurements performed at 4 K [Fig. 6(b)] reveal hysteresis loops for every sample. At higher temperatures the hysteresis loops are detected in samples annealed for ≥20 ms only. The magnetic moment per implanted Fe (μ_B/Fe) ion is much lower than that of bcc-Fe (2.2μ_B) and iron nitrides (e.g., 1.9μ_B for ε-Fe_3N).

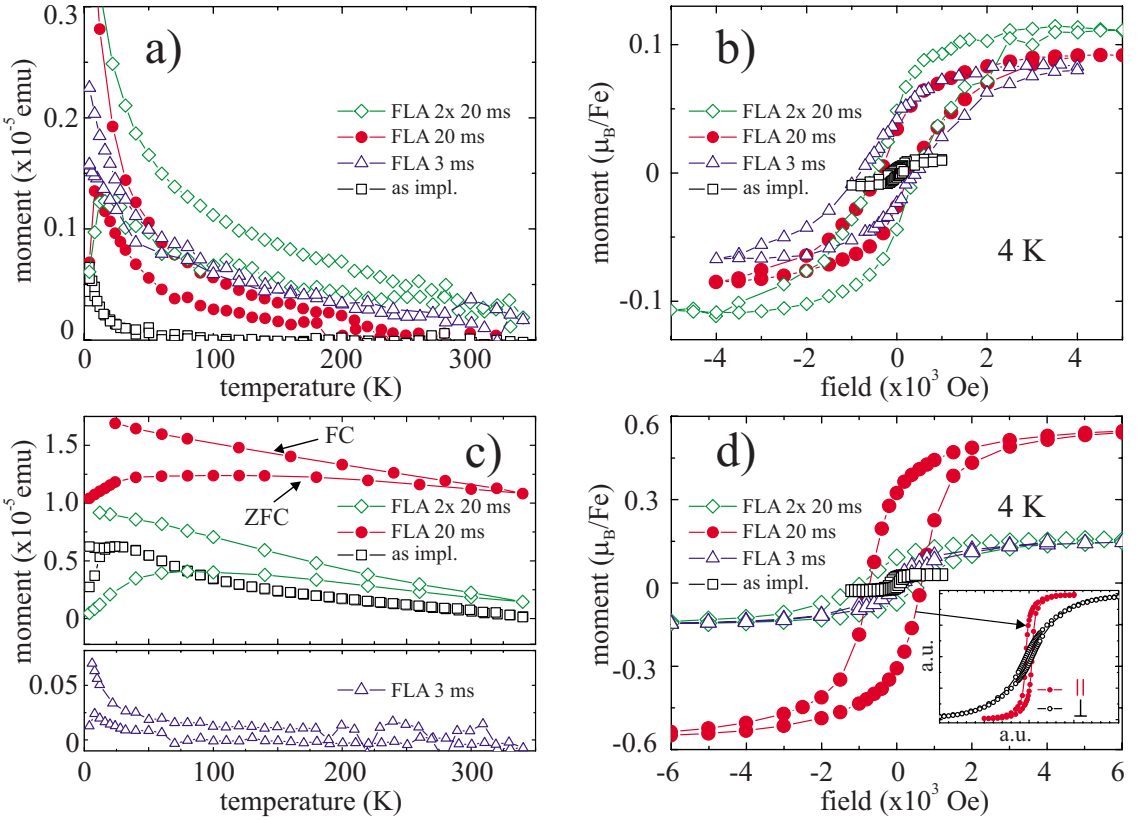

FIG. 6. (Color online) Field-cooled/zero-field-cooled (FC/ZFC) measurements performed at 50 Oe on the samples implanted with (a) 8×10^{16} cm^{-2} and (c) 1.6×10^{17} cm^{-2} and subsequently annealed samples. The field dependent magnetization curves of the respective samples (b) and (d) were recorded at 4 K. The inset in (d) reveals the magnetic anisotropy of the 1.6×10^{17} cm^{-2} implanted and 20 ms annealed sample.

The FC/ZFC scan of the as-implanted sample 2 [Fig. 6(c)] exhibits a shape similar to a spin glass. The magnetization measurement at 4 K [Fig. 6(d)] shows a hysteresis loop. At higher temperatures an S-like shape, i.e., no coercivity, is observed (not shown). It is remarkable, that in the CEM spectrum at 4.2 K no magnetic component was detected. This means that no ferro- or antiferromagnetic Fe-related secondary phase is present in the sample. Hence, the present state is attributed to the spinodal decomposition with concurrent local weak ferromagnetic and antiferromagnetic coupling of the constituents. The weak hyperfine fields cannot be resolved with CEMS. Moreover, assuming that the hysteresis *is* related to ferromagnetic bcc-Fe, only about 1% of total Fe amount ($0.025\mu_B$/Fe for the as-implanted sample 2 related to $2.2\mu_B$ for bcc-Fe) would contribute to the ferromagnetic response. This is in the range of CEMS noise.

After 3 ms annealing the shape of the FC/ZFC curve is not related to the spin-glass anymore. The curves are well separated [Fig. 6(c)]. Unfortunately, the magnetization value is of the order of magnitude of the SQUID error. The shape of the FC/ZFC curve as well as the presence of the hysteresis loop give a hint for the precipitation of a secondary phase. During 20 ms annealing the size of clusters increase dramatically and the size distribution becomes broader. This can be observed as the local maximum of the ZFC curve moves toward higher temperature and broadens. Taking into account the relative area of the ferromagnetic component M1 from the respective CEM spectrum (~24%), the magnetic moment fits well to the value of metallic bcc-Fe. Measurements with the field applied in-plane as well as out-of-plane reveal magnetic anisotropy of the bcc-Fe-clusters, with the easy axis parallel to the sample surface (in plane) [see inset Fig. 6(d)]. The presence of the clusters was confirmed by XRD [see Fig. 1(b)]. Previous investigations showed the formation of textured bcc-Fe-clusters within crystalline GaN.[11]

Upon the 2×20 ms annealing the maximum of the ZFC curve is shifted back to lower temperature values and the magnetization decreases. Based on the findings from the AES, CEMS, and XRD results the oxidation of clusters as well as the transformation from bcc-Fe to ε-Fe_3N is the most reasonable explanation.

All samples are found to be highly electrically resistive. Hence, no transport measurements were performed. Channeling RBS measurements show about 15–20 % recovery of the bulk damage caused by the ion implantation after flash-lamp annealing (not shown). The surface damage was not reduced at all. Here, however, the surface roughness plays an important role in the characterization of surface damage.

IV. CONCLUSION

The presented investigations show the correlation between structural and magnetic properties of Fe-ion implanted GaN. Spinodal decomposition is the preliminary stage before

the formation of precipitates. Sato *et al.*[16] predicted high Curie temperatures and spinodal decomposition for a Mn concentration of about 20 at. %. In the present work, Fe concentrations between 9 and 18 at. % and even higher in the as-implanted state, were used. In the as-implanted state spinodal decomposition seems to be responsible for the complex magnetic interaction, including the ferromagnetic as well as the antiferromagnetic one. The situation is even more complex, if the strong damage of the crystalline GaN after implantation is taken into account.

In annealed samples ferromagnetic response is related to different types of secondary phases. The type of the secondary phase depends on the dopant concentration and on the duration and/or temperature of thermal treatment.

Ion implantation can be successfully applied to oversaturate host materials with impurities up to a rather high concentration, however, regarding the high damage level produced in highly doped GaN it is less suitable technique with respect to DMS engineering. The flash-lamp annealing technique turned out to be a very suitable method for the production of metastable phases.

ACKNOWLEDGMENTS

G.T. acknowledges T. Schumann for carrying out the flash-lamp annealing. G.T. and F.S. acknowledge financial support by the Deutsche Forschungsgemeinschaft (German Research Foundation) under Contracts No. Re 868/8-2 and No. Ke273/19-2. We are thankful to W. Keune for the critical suggestions.

*g.talut@fzd.de

[1] T. Dietl, H. Ohno, and F. Matsukura, Phys. Rev. B **63**, 195205 (2001).
[2] K. Sato and H. Katayama-Yoshida, Jpn. J. Appl. Phys., Part 2 **40**, L485 (2001).
[3] K. Sato and H. Katayama-Yoshida, Semicond. Sci. Technol. **17**, 367 (2002).
[4] T. Dietl, Phys. Rev. B **77**, 085208 (2008).
[5] W. Pacuski, P. Kossacki, D. Ferrand, A. Golnik, J. Cibert, M. Wegscheider, A. Navarro-Quezada, A. Bonanni, M. Kiecana, M. Sawicki, and T. Dietl, Phys. Rev. Lett. **100**, 037204 (2008).
[6] A. Bonanni, M. Kiecana, C. Simbrunner, T. Li, M. Sawicki, M. Wegscheider, M. Quast, H. Przybylińska, A. Navarro-Quezada, R. Jakieła, A. Wolos, W. Jantsch, and T. Dietl, Phys. Rev. B **75**, 125210 (2007).
[7] S. Kuwabara, T. Kondo, T. Chikyow, P. Ahmet, and H. Munekata, Jpn. J. Appl. Phys., Part 2 **40**, L724 (2001).
[8] N. Theodoropoulou, A. F. Hebard, S. N. G. Chu, M. E. Overberg, C. R. Abernaty, S. J. Pearton, R. G. Wilson, and J. M. Zavada, J. Appl. Phys. **91**, 7499 (2002).
[9] Y. Shon, Y. H. Kwon, Y. S. Park, Sh. U. Yuldashev, S. J. Lee, C. S. Park, K. J. Chung, S. J. Yoon, H. J. Kim, W. C. Lee, D. J. Fu, T. W. Kang, X. J. Fan, Y. J. Park, and H. T. Oh, J. Appl. Phys. **95**, 761 (2004).
[10] Y. Shon, Sejoon Lee, H. C. Jeon, Y. S. Park, D. Y. Kim, T. W. Kang, Jin Soak Kim, Eun Kyu Kim, D. J. Fu, X. J. Fan, Y. J. Park, J. M. Baik, and J. L. Lee, Appl. Phys. Lett. **89**, 082505 (2006).
[11] G. Talut, H. Reuther, A. Mücklich, F. Eichhorn, and K. Potzger, Appl. Phys. Lett. **89**, 161909 (2006).
[12] T. Li, C. Simbrunner, A. Navarro-Quezada, M. Wegscheider, M. Quast, D. Litvinov, D. Gerthsen, and A. Bonanni, J. Cryst. Growth **310**, 3294 (2008).
[13] A. Bonanni, A. Navarro-Quezada, T. Li, M. Wegscheider, Z. Matěj, V. Holý, R. T. Lechner, G. Bauer, M. Rovezzi, F. D'Acapito, M. Kiecana, M. Sawicki, and T. Dietl, Phys. Rev. Lett. **101**, 135502 (2008).
[14] G. Talut, H. Reuther, Shengqiang Zhou, K. Potzger, F. Eichhorn, and F. Stromberg, J. Appl. Phys. **102**, 083909 (2007).
[15] Part of the SRIM program package by J. F. Ziegler at http://www.srim.org/
[16] K. Sato, H. Katayama-Yoshida, and P. Dederichs, Jpn. J. Appl. Phys., Part 2 **44**, L948 (2005).
[17] D. Panknin, J. Stoemenos, M. Eickhoff, V. Heera, M. Voelskow, and W. Skorupa, Appl. Surf. Sci. **184**, 377-382 (2001).
[18] R. A. Brand, Nucl. Instrum. Methods Phys. Res. B **28**, 398 (1987).
[19] A. Yu. Azarov, J. Jensen, A. Hallén, and T. Aggerstam, J. Appl. Phys. **104**, 053509 (2008).
[20] A. Bchetnia, C. Saidi, M. Souissi, T. Boufaden, and B. El Jani, Semicond. Sci. Technol. **24**, 095020 (2009).
[21] S. O. Kucheyev, J. S. Williams, and S. J. Pearton, Mater. Sci. Eng. **33**, 51 (2001).
[22] S. O. Kucheyev, J. E. Bradby, C. P. Li, S. Ruffell, T. van Buuren, and T. E. Felter, Appl. Phys. Lett. **91**, 261905 (2007).
[23] M. Ishimaru, Y. Zhang, and W. J. Weber, J. Appl. Phys. **106**, 053513 (2009).
[24] L. M. Lin, Yi Luo, P. T. Lai, and Kei May Lau, Thin Solid Films **515**, 2111 (2006).
[25] M. Borowski, A. Traverse, and J.-P. Eymery, Nucl. Instrum. Methods Phys. Res. B **122**, 247 (1997).
[26] P. Schaaf, Hyperfine Interact. **111**, 113 (1998).
[27] A. Shalimov, K. Potzger, D. Geiger, H. Lichte, G. Talut, A. Misiuk, H. Reuther, F. Stromberg, Shengqiang Zhou, C. Baehtz, and J. Fassbender, J. Appl. Phys. **105**, 064906 (2009).